10.24352/UB.OVGU-2018-003 TECHNISCHE MECHANIK, 38, 1, (2018), 3 - 21
submitted: July 31, 2017

An Experimental-numerical Study on the Plastic Flow Localization Based on a Generalized Micromorphic Formulation

E. Diamantopoulou, C. Labergere, K. Saanouni, B. Guelorget, M. François

Abstract

An experimental-numerical study based on simple plane strain tensile tests of a high strength metallic sheet is presented. The development of an 'advanced' modelling of multiphysic thermomechanical coupling in the framework of the generalized continuum mechanics (micromorphic theory) is already proposed in published works in order to introduce the concept of internal lengths that are representative of the material's microstructure while accounting for the various initial and induced anisotropies under large plastic strains. These internal lengths have to be experimentally determined from accurate measurements of highly localized displacement/strain (or velocity/strain rate) fields by using advanced methods to measure the kinematic fields at the relevant scales. We seek to locally measure the displacement and velocity fields in order to access to the local strain/strain rate fields inside the localized zones. Attention is paid to the prediction of the plastic flow and damage localization into narrow shear bands (localized necking) which follows the diffuse necking stage. The effect of the micromorphic material properties which define the intrinsic characteristic internal length on the evolution of these highly localized shear bands regarding the mesh size is deeply investigated. The numerical work is based on an advanced numerical methodology developed for metal forming simulations including thermodynamically-consistent nonlocal constitutive equations accounting for various fully coupled mechanical phenomena under finite strains in the framework of the micromorphic continua. The numerical implementation into ABAQUS/Explicit software is made thanks to VUMAT user's subroutine for the implementation of the micromorphic constitutive equations and the VUEL user's subroutine for 2D quadrilateral assumed strain elements with an additional micromorphic degree of freedom related to the micromophic damage.

1 Introduction

Nowadays, the fully local constitutive equations have been well established to model the induced material softening behaviour due to thermal, damage and other microstructure-dependent phenomena. However, the solutions of the associated fully local initial and boundary value problem are highly sensitive to the space and time discretization. The mechanics of generalized continua makes possible the straightforward introduction of the characteristic lengths into the constitutive equations of materials with microstructure in order to overcome this drawback (Saanouni and Hamed, 2013).
The most recent and comprehensive review of these generalized continua and their use to solve various problems in mechanics of solids and fluids is found in the books by Eringen (Eringen, 1999; Eringen, 2002; Forest, 2006; Saanouni, 2012). Based on these works, various generalized continuum theories have been introduced during the last decades in order to account for some effects of characteristic lengths related to the materials microstructure and leading to a wide range of models (Sidoroff, 1975; Maugin, 1979; Aifantis, 1987; Forest et al., 2002; Aifantis, 2003; Forest and Sievert, 2003; Liebe et al., 2003; Anandet. et al, 2005; Kirchner and Steinmann, 2005; Forest, 2006; Forest and Sievert, 2006; Forest, 2008; Forest, 2009; Hirschberger and Steinmann, 2009; Forest and Aifantis, 2010 among many others).
As summarized by Forest, all these generalized continuum theories, which are still based on the assumption of local action (Truesdell and Noll, 2004), can be classified into two classes: (i) the higher grade continua and (ii) the higher order continua. Higher grade continua are those based on higher order spatial derivatives of the displacement field as originally proposed by Mindlin (Mindlin, 1965; Mindlin and Eshel, 1968). While, higher

order continua are based on the introduction of additional degrees of freedom as pioneered by the Cosserat brothers (Cosserat, 1896, 1909, 2009) and extensively developed by Eringen and his co-workers in 1960s (Eringen and Suhubi, 1964; Eringen, 1966a, 1966b, 1970, 1999). A third class of generalized continuum theories is the so called strictly nonlocal continuum field theories, well summarized in the recent book by Eringen (Eringen, 2002) where a unified foundation of the basic field equations are presented and various main contributing works in the field are referenced.

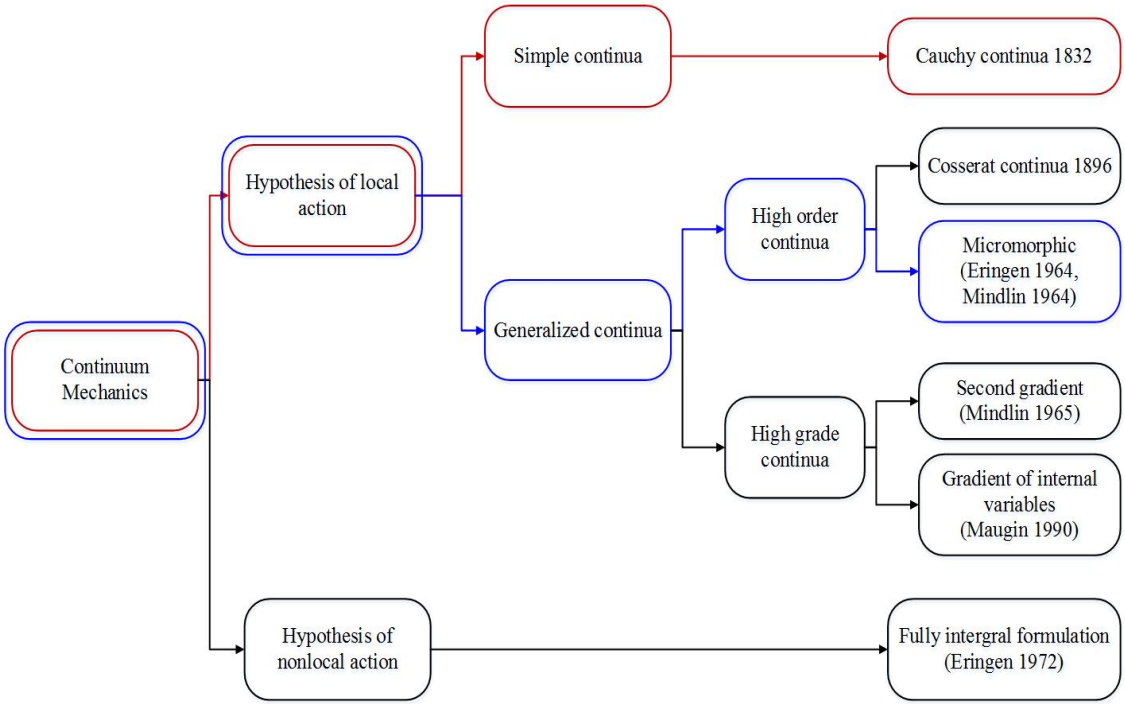

Figure 1. Schematics of the different theories in the mechanics of continuous media, Saanouni, (2012)

The micromorphic theory was initially proposed simultaneously by (Eringen and Suhubi, 1964; Mindlin, 1964). It consists of introducing a general non-compatible full field of micro-deformation as an extra degree of freedom, in addition to the classical displacement field. The micromorphic approach can, in fact, be applied to any macroscopic quantity in order to introduce a characteristic length scale in the original classical continuum model in a systematic way, as presented by (Saanouni and Hamed, 2012; Forest, 2009). From the comparison between nonlocal and micromorphic theories, Forest and Aifantis (Forest and Aifantis, 2010) concluded that when the micromorphic variable remains as close as possible to the plastic strain, the micromorphic model reduces to the strain gradient theory.

The main goal of this paper is to propose a methodology for the identification of the internal length related to the micromorphic damage. According to the analytical-experimental study described later, an experimental-numerical study is performed in order to determine the values of $\breve{H}$ and $\breve{H}^g$ and verify the characteristic length for each material and mesh size in total agreement with the experiments and the information extracted by Fig. 8.
The concept of internal lengths, that has to be experimentally determined from accurate measurements by using advanced photomechanical methods, is introduced.
From the numerical point of view, the introduction of the new balance equation in the micromorphic model carrying the effect of the ductile damage, demands the construction of an element based on an assumed strain formulation combined with an extension of the Hu-Washizu mixed variational form. The standard B matrix obtained from the displacement field analytically and including the hourglass control part, is projected to eliminate volumetric and shear locking phenomena.
This kind of micromorphic elastoplastic constitutive equations with damage can be later used for the numerical simulation of various sheet and bulk metal forming processes.

2 Theoretical Aspects

2.1 The generalized Principle of Virtual Power

The virtual power of internal forces is extended for a micromorphic continuum by using the virtual micromorphic damage (Saanouni, 2012; Saanouni and Hamed, 2013):

$$P_{\text{int}}\left(\vec{u}^*,\breve{d}^*\right)=-\int_V\left(\underline{\sigma}:\left(\vec{\nabla}\dot{\vec{u}}\right)^*+\breve{Y}\dot{\breve{d}}^*+\vec{\breve{Y}}\cdot\nabla\dot{\breve{d}}^*\right)dV \tag{1}$$

where, $\underline{\sigma}$ is the Cauchy stress tensor, the scalar $\breve{Y}$ and vector $\vec{\breve{Y}}$ are the stress-like variables with respect to micromorphic damage $\breve{d}$ and its first gradient $\vec{\nabla}\breve{d}$.

Similarly, the virtual power of external forces is also extended by adding the generalized body forces $\vec{f}^u$, $f^{\breve{d}}$, $\vec{f}^{g\breve{d}}$ and the contact forces $\vec{F}^u$ and $F^{\breve{d}}$ associated with the kinematic variables and their first gradients:

$$P_{ext}\left(\vec{u}^*,\breve{d}^*\right)=\rho\int_V\left(\vec{f}^u\cdot\dot{\vec{u}}^*+f^{\breve{d}}\dot{\breve{d}}^*+\vec{f}^{g\breve{d}}\cdot\vec{\nabla}\dot{\breve{d}}^*\right)dV+\int_\Gamma\left(\vec{F}^u\cdot\dot{\vec{u}}^*+F^{\breve{d}}\dot{\breve{d}}^*\right)dS \tag{2}$$

The virtual power of the inertia forces is enhanced by a new micromorphic contribution according to:

$$P_a\left(\vec{u}^*,\breve{d}^*\right)=\rho\int_V\left(\ddot{\vec{u}}\cdot\dot{\vec{u}}^*+\zeta_{\breve{d}}\ddot{\breve{d}}\dot{\breve{d}}^*\right)dV \tag{3}$$

where, $\zeta_{\breve{d}}$ is a scale factor which maps the local material density to the micromorphic level (Nedjar, 2001; Saanouni, 2012; Saanouni and Hamed, 2013).

For any kinematically admissible virtual fields, the generalized micromorphic virtual power is written under the following form:

$$P_{\text{int}}+P_{ext}=P_a\qquad\forall\vec{u}^*,\breve{d}^*\ K.A. \tag{4}$$

By using Eq. (1) - Eq. (3) and using the divergence theorem to transform the volume integrals, Eq. (4) leads to two balance equations together with their Neumann boundary conditions. The first one is the standard and well known local balance of momentum:

$$\begin{cases}\vec{\nabla}\cdot\underline{\sigma}+\rho\vec{f}^u=\rho\ddot{\vec{u}} & in\ \Omega\\ \underline{\sigma}\cdot\vec{n}=\vec{F}^u & on\quad\Gamma\end{cases} \tag{5a}$$

and the second one is an additional generalized micromorphic balance of momentum:

$$\begin{cases}\left(\vec{\nabla}\cdot\vec{\breve{Y}}+\breve{Y}\right)+\rho\left(f^{\breve{d}}-\vec{\nabla}\cdot\vec{f}^{g\breve{d}}\right)=\rho\zeta_{\breve{d}}\ddot{\breve{d}} & in\ \Omega\\ \left(\vec{\breve{Y}}-\rho\vec{f}^{g\breve{d}}\right)\cdot\vec{n}=F^{\breve{d}} & on\quad\Gamma\end{cases} \tag{5b}$$

These two partial differential equations are considered as the strong forms of the Initial and Boundary Value Problem (IBVP) with respect to displacement and micromorphic damage fields. The stress-like variables $\underline{\sigma}$, $\breve{Y}$ and $\vec{\breve{Y}}$ will be defined by the state relations developed in the framework of thermodynamic of irreversible processes with appropriate state variables.

2.2 State Relations

In this section, a specific state potential is constructed for an isothermal isotropic elastoplastic model fully coupled with isotropic local damage, local isotropic and kinematic hardenings and isotropic micromorphic damage. The effective state variables are deduced from the local state variables according to the assumption of the total energy equivalence developed in (Saanouni et al., 1994; Saanouni et al., 2008; Saanouni and Hammi,

2000; Labergère et al., 2011; Issa et. al, 2012; Saanouni and Hamed, 2013; Badreddine et al., 2015). We assume, as for a classical local continuum, that the energy balance holds for a micromorphic medium of order one. For the sake of simplicity, we also postulate that only the local damage is coupled with the micromorphic damage. Under these assumptions, Helmholtz free energy can be expressed as a closed convex function of the overall (both local and micromorphic) strain-like state variables:

$$\rho\psi = \frac{1}{2}(1-d)\left(\underline{\varepsilon}^e : \underline{\underline{\Lambda}} : \underline{\varepsilon}^e + \frac{2}{3}C\underline{\alpha} : \underline{\alpha}\right) + \frac{1}{2}\left(\left(1-d^\gamma\right)Qr^2 + \breve{H}\left(d-\breve{d}\right)^2 + \breve{H}^g\vec{\nabla}\breve{d}\cdot\vec{\nabla}\breve{d}\right) \tag{6}$$

where $\underline{\underline{\Lambda}} = \lambda_e \underline{1}\otimes\underline{1} + 2\mu_e \underline{\underline{1}}$ is the positive definite symmetric fourth-rank elastic tensor defined by the classical Lame's parameters. C and Q are the macro moduli of the kinematic and the isotropic hardening respectively. $\breve{H}$ is the coupling modulus with respect to the micromorphic damage while $\breve{H}^g$ is the micromorphic modulus related to the micromorphic damage first gradient. Finally, γ is the parameter governing the effect of the local damage on the local isotropic hardening.
The local and micromorphic stress-like variables are derived under the following forms:

$$\underline{\sigma} = \rho\frac{\partial\psi}{\partial\underline{\varepsilon}^e} = (1-d)\underline{\underline{\Lambda}} : \underline{\varepsilon}^e = (1-d)\left(\lambda_e tr\left(\underline{\varepsilon}^e\right)\underline{1} + 2\mu_e\underline{\varepsilon}^e\right) \tag{7}$$

$$\underline{X} = \rho\frac{\partial\psi}{\partial\underline{\alpha}} = \frac{2}{3}(1-d)C\underline{\alpha} \tag{8}$$

$$R = \rho\frac{\partial\psi}{\partial r} = \left(1-d^\gamma\right)Qr \tag{9}$$

$$Y = -\rho\frac{\partial\psi}{\partial d} = \frac{1}{2}\left(\underline{\varepsilon}^e : \underline{\underline{\Lambda}} : \underline{\varepsilon}^e + \frac{2}{3}C\underline{\alpha} : \underline{\alpha} + \gamma d^{\gamma-1}Qr^2\right) - \breve{H}\left(d-\breve{d}\right) = Y^e + (Y^\alpha + Y^r + \breve{Y}) \tag{10}$$

$$\breve{Y} = \rho\frac{\partial\psi}{\partial\breve{d}} = -\breve{H}\left(d-\breve{d}\right) \tag{11}$$

$$\vec{\breve{Y}} = \rho\frac{\partial\psi}{\partial\vec{\nabla}\breve{d}} = \breve{H}^g\vec{\nabla}\breve{d} \tag{12}$$

The damage dual stress-like force given in Eq. (10) can be decomposed into local part and coupled nonlocal part with the help of the micromorphc state relations Eq. (11) and Eq. (12):

$$\begin{cases} Y = Y_{loc} + Y_{nloc} \\ Y_{loc} = \frac{1}{2}\left(\underline{\varepsilon}^e : \underline{\underline{\Lambda}} : \underline{\varepsilon}^e + \frac{2}{3}C\underline{\alpha} : \underline{\alpha} + \gamma d^{\gamma-1}Qr^2\right) \\ Y_{nloc} = \breve{Y} = -\breve{H}\left(d-\breve{d}\right) \end{cases} \tag{13}$$

It is worth noting that if the micromorphic effects are neglected, i.e., $\breve{H} = \breve{H}^g = 0$, the micromorphic state variables given by Eqs. (11) - (12) are zero leading to zero contribution of the nonlocal terms. In that case the classical fully coupled local state relations originally given in (Saanouni, Forster, Benhatira, 1994; Saanouni, 2012) are integrally recovered.

2.3 Evolution Equations

The intrinsic dissipation remains under a purely local form without the direct contribution of any micromorphic phenomenon since we assume that the micromorphic variables do not dissipate. This assumption is made mainly due to the absence of any experimental information about the dissipation of the micromorphic phenomena.
Since there's no micromorphic damage dissipation, to account for the damage effects, we limit ourselves to the isotropic plasticity for simplicity. The von Mises yield function and dissipation potentials used in (see Saanouni, et al., 1994, 2008; Saanouni and Hammi, 2000; Labergère et al., 2011; Issa et. al, 2012; Saanouni and Hamed, 2013; Badreddine et al., 2015) are considered:

$$f\left(\underline{\sigma},\underline{X},R;d\right)=\frac{\left\|\underline{\sigma}-\underline{X}\right\|}{\sqrt{1-d}}-\frac{R}{\sqrt{1-d^{\gamma}}}-\sigma_{y}\leq 0 \tag{14}$$

$$F\left(\underline{\sigma},\underline{X},R,d\right)=f+\frac{3}{4}\frac{a\underline{X}:\underline{X}}{C\left(1-d\right)}+\frac{1}{2}\frac{bR^{2}}{Q\left(1-d^{\gamma}\right)}+\frac{S}{\left(s+1\right)\left(1-d\right)^{\beta}}\left\langle\frac{Y-Y_{0}}{S}\right\rangle^{(s+1)} \tag{15}$$

where, $\left\|\underline{\sigma}-\underline{X}\right\|=\sqrt{(3/2)(\underline{\sigma}^{dev}-\underline{X}):(\underline{\sigma}^{dev}-\underline{X})}$ defines the well-known von Mises equivalent stress and $\underline{\sigma}^{dev}$ is its deviatoric part of the stress tensor. The parameters α and b reflect the nonlinear property of the kinematic and isotropic hardening respectively and S, s and β characterize the nonlinear evolution of the ductile damage. Clearly, the yield function and plastic potential are identical to the local theory. However, the indirect contribution of the micromorphic state variables is introduced from the state relations. Applying the generalized normality rule to the above defined local yield function and dissipation potential lead to the following evolution equations:

$$\underline{\dot{D}}^{p}=\dot{\lambda}\frac{\partial F}{\partial\underline{\sigma}}=\dot{\lambda}\underline{\tilde{n}}=\dot{\lambda}\frac{\underline{n}}{\sqrt{1-d}} \tag{16}$$

$$\underline{\dot{\alpha}}=-\dot{\lambda}\frac{\partial F}{\partial\underline{X}}=\dot{\lambda}\left(\frac{\underline{n}}{\sqrt{1-d}}-a\underline{\alpha}\right) \tag{17}$$

$$\dot{r}=-\dot{\lambda}\frac{\partial F}{\partial R}=\dot{\lambda}\left(\frac{1}{\sqrt{1-d^{\gamma}}}-br\right) \tag{18}$$

$$\dot{d}=\dot{\lambda}\frac{\partial F}{\partial Y}=\frac{\dot{\lambda}}{(1-d)^{\beta}}\left(\frac{\left\langle(Y_{loc}+Y_{nloc})-Y_{0}\right\rangle}{S}\right)^{s} \tag{19}$$

where $\underline{n}=\dfrac{\partial f}{\partial\underline{\sigma}}$ is the outward normal to the yield surface in the rotated stress space and $\underline{\tilde{n}}=\dfrac{\partial f}{\partial\underline{\tilde{\sigma}}}$ is the same normal but expressed in the effective rotated stress space. The plastic multiplier $\dot{\lambda}$ appearing in all the evolution equations given above is deeply affected by the micromorphic variables linking it to a nonlocal nature.

In this case of time independent plasticity, $\dot{\lambda}$ is classically deduced from the consistency condition applied to the yield function (Eq. (14)): $\dot{f}\left(\underline{\sigma},\underline{X},R;d\right)=0$ if $f\left(\underline{\sigma},\underline{X},R;d\right)=0$. However, this is not necessary since the plastic miltiplier will be compluted numerically at each integration point in order to ensure the plastic admissibility condition.

The plastic multiplier $\dot{\lambda}$ appearing in all the evolution equations is deduced from the consistency condition applied to the yield function Eq.(14): $\dot{f}\left(\underline{\sigma},\underline{X},R;d\right)=0$ giving the following closed form expression:

$$\dot{\lambda}=\frac{1}{H_{p}}\left(\sqrt{1-d}\,\underline{n}:\underline{\underline{\Lambda}}:\underline{D}\right) \tag{20}$$

where, H_{p} is the generalized elastoplastic hardening modulus.

2.4 Transformation of the Micromorphic Balance Equations

Considering the generalized balance equation of micromorphic momentum Eq. (5b), it can be easily expressed in strain-like variables space by using micromorphic state relations Eq. (11) and Eq. (12):

$$\begin{cases}\left(\breve{H}^{g}Lap\left(\breve{d}\right)-\breve{H}\left(d-\breve{d}\right)\right)+\rho\left(f^{\breve{d}}-\vec{\nabla}\cdot\vec{f}^{g\breve{d}}\right)=\rho\zeta_{D}\ddot{\breve{d}} & in\ \Omega\\ \left(\breve{H}^{g}\left(\vec{\nabla}\breve{d}\right)-\rho\vec{f}^{g\breve{d}}\right)\cdot\vec{n}=F^{\breve{d}} & on\ \Gamma\end{cases} \tag{21}$$

By neglecting the micromorphic body and contact forces, i.e. $f^{\breve{d}}=0$, $\vec{f}^{g\breve{d}}=0$ and $F^{\breve{d}}=0$, the above equation can take the following form:

$$\begin{cases} l_{\breve{d}}^2 Lap\left(\breve{d}\right)+\left(d-\breve{d}\right)=\rho\dfrac{\zeta_{\breve{d}}}{\breve{H}}\ddot{\breve{d}} & in\ \Omega \\ \left(\breve{H}^g\left(\vec{\nabla}\breve{d}\right)\right)\cdot\vec{n}=0 & on\ \Gamma \end{cases} \tag{22}$$

where, $l_{\breve{d}}$ is the intrinsic internal length scale parameter related to the micromorphic damage defined as square root of the ratio of the two micromorphic moduli:

$$l_{\breve{d}}=\sqrt{\frac{\breve{H}^g}{\breve{H}}} \tag{23}$$

Eq. (22) is preferred to be used as the strong form from which the associated weak form will be deduced right after in order to solve the fully coupled IBVP. If the micromorphic damage inertia is neglected (i.e., $\zeta_{\breve{d}}=0$) in the micromorphic damage balance equation, leads to the well-known Helmholtz equation proposed in the framework of the so called implicit nonlocal damage formulation proposed in (Engelen et al., 2003; Geers, 2004; Geers et al;, 2003).

3 Numerical Aspects

In this section, an advanced numerical procedure is presented. The finite element code that is used to implement the micromorphic model is developed in ABAQUS®. This numerical approach consists of: (i) the global resolution of the two balance equations (i.e. classical mechanical and micromorphic damage equilibrium equations) and (ii) the local integration of the overall fully coupled constitutive equations on each integration point of each element, which is necessary to calculate the internal forces appearing in the weak forms associated to the balance equations.
The numerical integration, mixed for one/four quadrature(s) (or Gauss) points for all the coupled constitutive equations, is necessary in order to compute the stress tensor and the overall stress-like internal variables appearing in the weak forms. The local integration algorithm consists of discretizing all the constitutive equations through the time interval $t_n \le t \le t_{n+1}=t_n+\Delta t$ and calculating the values of all the mechanical fields at the end of the increment t_{n+1} while the loading increment $\Delta\underline{\varepsilon}=\Delta t\underline{D}_{n+1}$ as well as the values of all the fields at the beginning of the time increment t_n are known. For the time discretization of the equations of this behavior model, the fully implicit (iterative) Euler scheme in combination with an asymptotic one applied to the hardening equations are chosen (Saanouni, 2012). The overall constitutive equations are then reduced to two nonlinear and strongly coupled algebraic equations with two unknowns: $\Delta\lambda$ and d_{n+1}. For each integration point concerned by the plastic flow, the iterative method of elastic prediction-plastic correction is used to integrate numerically the complete set of constitutive equations thanks to a Newton-Raphson resolution procedure in order to converge towards a point lying on the current loading surface. The constitutive equations defined in the framework of the micromorphic continua are implemented into ABAQUS®/Explicit thanks to the VUMAT user's subroutine.
An element with the additional micromorphic degree of freedom concerning the micromorphic damage is implemented using the VUEL user's subroutine as discussed here after.

The introduction of the new micromorphic balance equation in the behaviour model with micromorphic damage demands the construction of a special element based on a mixed variational form and having $\breve{d}$ as the additional degree of freedom (d.o.f). Fish and Belytschko (Belytscho, 2000) proposed an extension of the Hu-Washizu weak form of the variational principle in nonlinear mechanics of solids. We consider two variational forms and introduce the balance equation with the contribution of the micromorphic damage discretized on a domain **Ω**.
The weak form of the balance equations can be obtained thanks to the weighted residual method (Belytscho, 2000) in order to get:

$$\begin{cases} \int_\Omega \underline{\sigma}_a : \delta\underline{\varepsilon}_a d\Omega + \delta\int_\Omega \underline{\sigma}_a : \left(\vec{\nabla}^{sym}(\vec{u}) - \underline{\varepsilon}_a\right) d\Omega - \delta W_{ext} = 0 \\ \int_\Omega \left(\breve{d}\delta\breve{d} + \ell_d^2(\vec{\nabla}\breve{d}).(\vec{\nabla}\delta\breve{d})\right) d\Omega - \int_\Omega \left(d\delta\breve{d}\right) d\Omega = 0 \end{cases} \tag{24}$$

where δW_{ext} is the external forces virtual work, δ represents the classical variation operator, $\vec{u}$ is the displacement vector, $\underline{\sigma}$ the Cauchy stress tensor, $\underline{\varepsilon}_a$ the tensor of the assumed strains, $\underline{\sigma}_a$ the assumed stress tensor and $\underline{\nabla}^s(\vec{u})$ is the symmetric part of the displacement gradient. Simo and Hughes (Simo and Hughes, 1998) suggested the the projection of the discretized gradient $\left[B^e_{n+1/2}\right]$ of the velocity field. This new operator is chosen in order to evaluate the assumed strain tensor $\left\{\varepsilon^a\right\}_{n+1} = \left[B^e_{n+1/2}\right]\left\{u^e\right\}_{n+1/2}$ and to compute the associated assumed stress tensor $\left\{\sigma^a_{n+1}\right\}$ which is orthogonal to the difference between the symmetric part of the velocity gradient and the assumed strain tensor. This choice allows us to simplify the Hu-Washizu weak form as follows:

$$\begin{cases} \int_\Omega \underline{\sigma}_a : \delta\underline{\varepsilon}_a d\Omega - \delta W_{ext} = 0 \\ \int_\Omega \left(\breve{d}\delta\breve{d} + \ell_d^2(\vec{\nabla}\breve{d}).(\vec{\nabla}\delta\breve{d})\right) d\Omega - \int_\Omega \left(d\delta\breve{d}\right) d\Omega = 0 \end{cases} \tag{25}$$

Wang (Wang et al., 2006) proposed the construction of a quadrangular element to the field of the assumed strains in a 2D plane strain in order to control the shear and volumetric locking. The isoparametric shape functions for the 4-node quadrilateral can be written in terms of a set of orthogonal base vectors as:

$$N_i(\xi,\eta) = \frac{1}{4}\mathbf{s} + \frac{1}{4}\boldsymbol{\xi}\xi + \frac{1}{4}\boldsymbol{\eta}\eta + \frac{1}{4}\mathbf{h}\xi\eta \tag{26}$$

where (ξ,η) are the coordinates in the reference space with $\boldsymbol{\xi}^T = [-1,1,1,-1]$, $\boldsymbol{\eta}^T = [-1,-1,1,-1]$, $\mathbf{s}$ is the translation vector with $\mathbf{s} = [1,1,1,1]$ and $\mathbf{h}$ is the hourglass vector with $\mathbf{h} = [1,-1,1,-1]$.

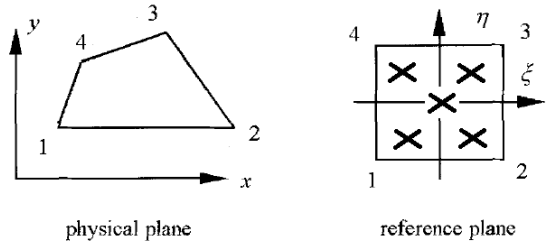

Figure 2. A 4-node quadrilateral element in physical and natural coordinate systems, Wang (2004)

To this element we have added the degree of freedom associated to the micromorphic damage. In order to avoid any objectivity-related problems, a local corotational system is built in the centroid of the element (see Fig.3) using the shape functions defined in the reference space (ξ,η). The orientation of this corotational triad is governed by the orthogonal rotation tensor $\underline{Q}$ which is expressed under the following form:

$$[Q] = \begin{bmatrix} e_1^1 & e_1^2 \\ e_2^1 & e_2^2 \end{bmatrix},\ \vec{g}_1 = \frac{\partial x}{\partial\xi}\vec{x} + \frac{\partial x}{\partial\eta}\vec{y},\ \ \vec{e}_1 = \frac{\vec{g}_1}{\|\vec{g}_1\|},\ \ \vec{e}_2.\vec{e}_1 = 0,\ \|\vec{e}_2\| = 1 \tag{27}$$

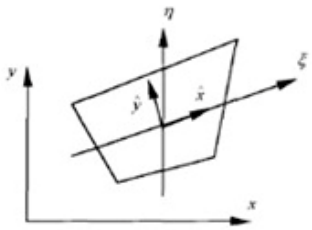

Figure 3. Corotational definition of the Q4-URI element, Wang, (2004)

The matrix $\left[B^{e}_{n+1/2}\right]$ is decomposed in two parts: $\left[B^{0}_{n+1/2}\right]$ which is constant and gives all the components of the strain tensor $\left\{\varepsilon^{a}\right\}_{n+1}$ in the centre of the element, and $\left[B^{h}_{n+1/2}\right](\xi,\eta)=\xi\left[B^{\xi}_{n+1/2}\right]+\eta\left[B^{\eta}_{n+1/2}\right]$ for the components of the same tensor at the rest points of the element. The operators $\left(B^{\xi},B^{\eta}\right)$ are called anti-hourglass strain matrices and are implemented in order to suppress the hourglass modes. Those high order terms can also be modified for the elimination of volumetric and shear locking phenomena.
Finally, the expression of the total strain tensor, according to the assumptions above, is written as follows:

$$\left\{\varepsilon^{a}\right\}_{n+1}=\left[B^{e}_{n+1/2}\right]\left\{u^{e}\right\}_{n+1/2}=\underbrace{\left[B^{0}_{n+1/2}\right]\left\{u^{e}\right\}_{n+1/2}}_{\left\{D^{0}\right\}_{n+1}}+\underbrace{\left[B^{h}_{n+1/2}\right]\left\{u^{e}\right\}_{n+1/2}}_{\left\{D^{h}\right\}_{n+1}}=\left\{\varepsilon^{0}\right\}_{n+1}+\left\{\varepsilon^{h}\right\}_{n+1} \tag{28}$$

4 Experimental Aspects

The study of the strain localization behavior from an experimental perspective using photomechanical methods is introduced. Electronic Speckle Pattern Interferometry (ESPI) has been used for the deformation measurement, because of its specific advantages, such as high spatial and displacement resolutions.
The principles of ESPI are simple: a speckle field, e.g. a seemingly random intensity pattern, is produced by the interference of the wave fronts, when a coherent light illuminates a rough diffusing surface. A micro-displacement or deformation of the object surface leads to changes of the speckle field and thus the deformation information can be obtained from the correlated evolution of the initial speckle pattern (Labergere et al., 2014, Guelorget et al., 2006). The experimental setup is represented in Fig. 4.

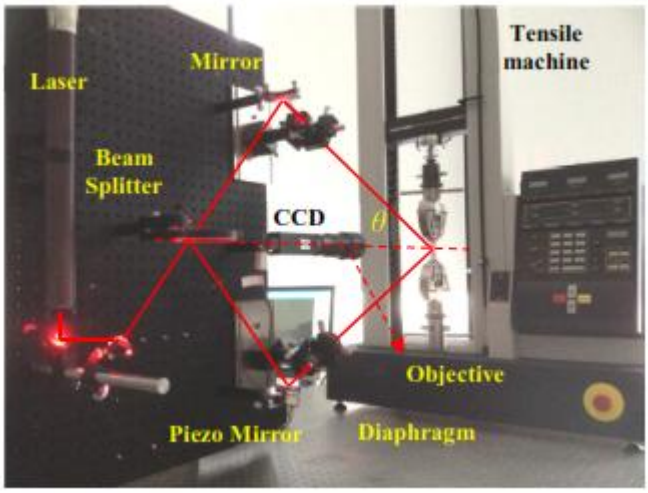

Figure 4. Experimental set-up: in-plane speckle interferometry. The laser beam path is schematized as a red line, (Bao, François, Le Joncour, 2015)

The specimens on which the tests were performed are made of steel 430 (X8Cr17) with effective length of 45 mm, width of 15 mm, and thickness of 0.2 mm, and cut along 45° with respect to the rolling direction (Fig. 5). The specimen was set in the tensile machine with the bottom clamp fixed, the top clamp lifted under controlled speed, which was kept constant at 0.5 mm/min in the early stage and decreased to 0.015 mm/min near and

beyond to the maximum load to observe precisely the state of localization. It should be pointed out that the tensile test evolution is monitored through the average total strain computed from the cross-beam displacement and the initial gauge length of the specimens as ln(L/L0).

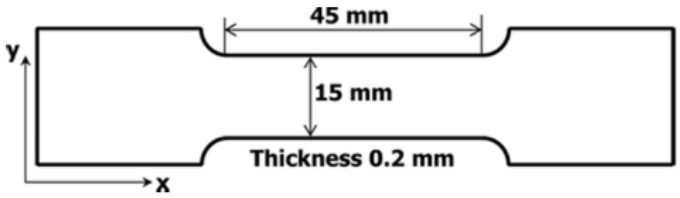

Figure 5. Specimen geometry and reference system 40x11mm (300 x 300 DPI)

The fringe patterns shown in Fig. 6 represent the displacement field increment between the capture of two phase maps separated by the duration indicated besides each picture. Constant and homogenous strain appears as a uniform fringe pattern in which fringes are straight and perpendicular to the tensile direction. So in the elastic and homogenous plastic deformation range, there is no change in the fringe pattern appearance. As soon as the plastic deformation becomes inhomogeneous, the fringes start to curve, with a non-uniform spacing, and concentrate in the middle of the specimen forming an hourglass shape which can be interpreted as two crossing localization bands, as can be seen in Figs. 6 and 7.

This hourglass shape narrows progressively and, around 23% average strain, turns into an “X” shape. The fringe spatial frequency is higher in the middle of the specimen than along the two edges of the specimen which means that the strain is higher in the middle. In the area outside the “X”, where there is no fringe, the material stops deforming plastically and undergoes elastic unloading when the force decreases. At the beginning of the localization, the hourglass shape is symmetric, and then it loses the symmetry when it turns into an “X”. Then the fringes (deformations) start to concentrate in one of the bands (or one of the branches of “X”), thus the other one tends to disappear gradually and finally the specimen breaks along the band left. The transition between the symmetric hourglass and the asymmetric “X” is interpreted as the onset of localized necking.

The localized necking stage can be divided into two sub-stages, one where the disappearing band is still active and another where it disappears (Fig. 6).

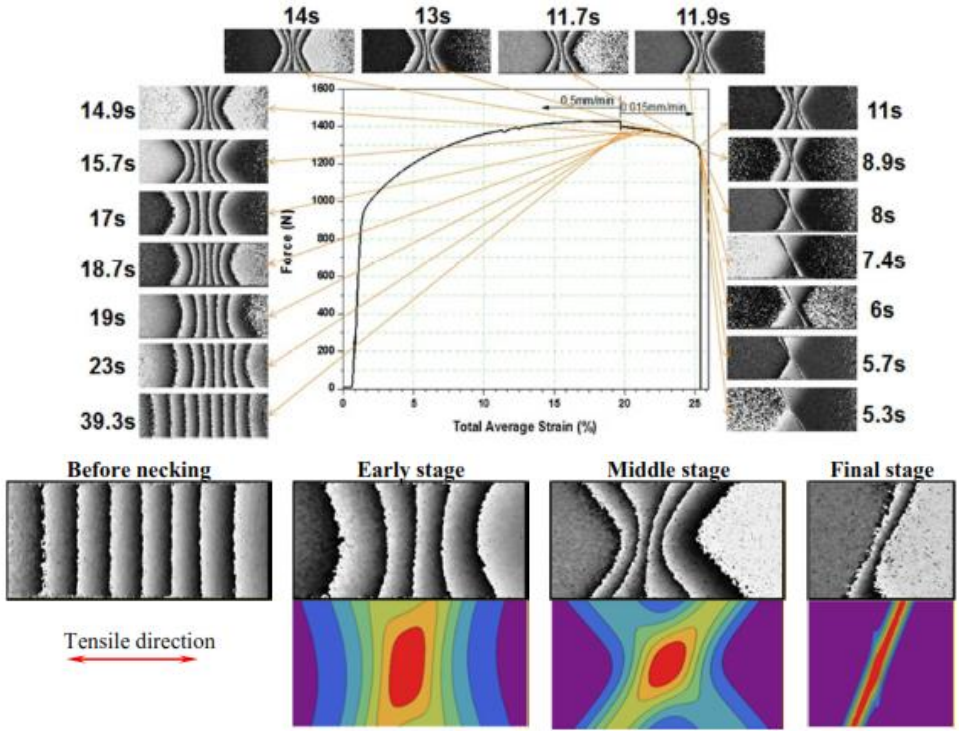

Figure 6. Evolutions of the fringe patterns (top row) obtained by ESPI and the corresponding strain rate maps (bottom row) during the reference test.

For extracting global information and physically relevant parameters, the strain rate pattern is modeled assuming that the strain rate field is a system of two straight crossing bands based on the “X” shape of the fringe pattern.

The strain rate distribution along each band is supposed to be constant. The whole strain rate distribution is assumed to be a simple superposition (sum) of the strain rate distribution of these two bands. This model is not a mechanical model but a purely geometric model used to describe the strain rate pattern and extract global parameters and completely independent of the constitutive behavior of the material. The strain rate distribution in each band is described by a linear combination of a Gaussian and a Lorentzian function:

$$\dot{\varepsilon}_{xx}(x,y) = \dot{\varepsilon}_1^{\max}(\eta_1 G_1 + (1-\eta_1)L_1) + \dot{\varepsilon}_2^{\max}(\eta_2 G_2 + (1-\eta_2)L_2) \tag{29}$$

where i = 1 or 2 indicates one of the two localized bands, and (x, y) are the coordinates of the points (x is parallel to the tensile direction), with:

- $\dot{\varepsilon}_i^{\max}$ is the maximum strain rate,
- G_i, Gaussian function,
- L_i, Lorentzian function,
- η_i and $1-\eta_i$ are the weights of the Gaussian and the Lorentzian functions respectively.

The Gaussian and Lorentzian functions are defined as following:

$$G(a,b,B,x,y)\exp(-\pi(\frac{x-ay-b}{B})^2) \tag{30}$$

$$L(a,b,B,x,y) = \frac{1}{1+(\pi\frac{x-ay-b}{B})^2} \tag{31}$$

- α, the inclination of the band with respect to the transverse direction,
- b, the location of the band,
- B, the integral width of the band.

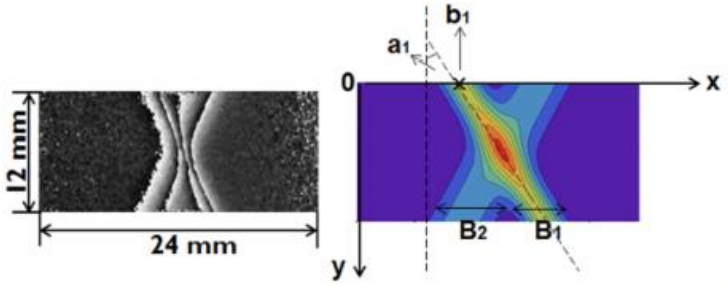

Figure 7. Illustration of the parameters, the image on the left is a fringe pattern and that on the right is the corresponding strain rate map obtained.

The inclination angles of the bands are defined as the angles between the band length and the tensile direction. The parameters of the model are identified by a least squares fitting procedure from the velocity maps obtained by ESPI.

The obtained evolution of the strain rate map is shown on Fig. 8 for a test at 0.015 mm/min. The evolutions with the global average strain of the widths of the bands are shown. In all cases, the specimens failed in the same direction, along the band that was oriented almost perpendicular to the rolling direction or along band 1 as illustrated in Fig. 7. Thereby for the sake of simplicity, this band will be called dominant band and the other one disappearing band, and the superscript “dom” and “dis” will be used to distinguish them.
On the strain rate maps evolution, the observations made on the fringe patterns are clearer. In a first stage, the maps exhibit a symmetric hourglass shape. In a second stage, defined as the localized necking, one band starts to predominate and the shape turns into an asymmetric “X” shape. The strain rate in the dominant band increases progressively until fracture.

The maximum strain rate of the band^{dom} increases exponentially with cross-beam displacement while the maximum strain rate of band^{dis} increases slowly and even starts to decrease close to the end of the test. During diffuse necking, the hourglass pattern formed by the two bands is symmetric and the maximum strain rates of the two bands are equal. Then, the strain rate of the two bands starts to diverge.

The bandwidths B of the two bands, in all cases, decrease with the total average strain or time. At the beginning, the two bandwidths decrease simultaneously and then they separate: B^{dis} tends to stabilize while B^{dom} continues decreasing.

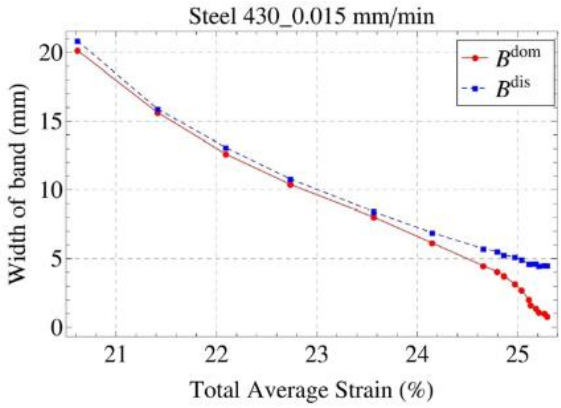

Figure 8. Evolutions of the localization bands widths vs total average strain (or time)

The bands widths of the two bands decrease at a similar rate during the diffuse necking. Then, when the localized necking stage starts, the width of the dominant band continues decreasing until the rupture, while the width of the disappearing band continues to decrease for a while and then stabilizes. Based on this observation, which is consistent with the strain rate evolutions, two sub-stages are distinguished in the localized necking regime. The transition of these two sub-stages is defined as the stabilization of the disappearing band width.

5 Numerical Results

5.1 Parametric Study of the Micromorphic Model

In this section we present a brief parametric study of the micromorphic model and more particularly the effect of the two parameters $(\breve{H}, \breve{H}^g)$ related to the micromorphic damage and the mesh size. We examine the role of each one of these two parameters on the quality of the numerical solution in terms of the force-displacement curves and the damage distribution in the totally damaged area. For this, we use the Q4 micromorphic elements described above, implemented in ABAQUS®/Explicit thanks to the VUEL user's subroutine and we compare the numerical results with those provided by the experiments.

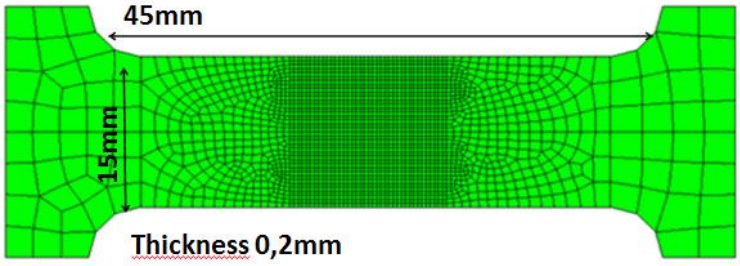

Figure 9. Geometry and mesh of the tensile specimen (Nnodes: 7502, Nelements: 7367)

The local parameters of the model are given in Table1 below.

E (GPa)	ν	σ_{yield} (MPa)	Q (MPa)	b	C (MPa)	a	S_T	DC	s	β	$\breve{H}$ (N)	$\breve{H}g$ (MPa)
220	0,3	300,0	1135, 0	2,0	3400,0	40,0	5,0	0.99	1,0	1,0	?	?

Table. 1: Material paremeters

In this case, all the phenomena are supposed to be local and only the damage is supposed to be micromorphic, giving one additional degree of freedom apart from the displacement, and one more balance equation. We also note that there is only one internal length related to the micromorphic damage which is taken into consideration given by Eq. (22).

For the first test case, we kept the internal length constant at $\ell_{\bar{d}} = 0,6\,mm$ by picking three different pairs of the micromorphic moduli, e.g., $(\breve{H} = 10, \breve{H}^g = 3,6)$, $(\breve{H} = 100, \breve{H}^g = 36)$ and $(\breve{H} = 1000, \breve{H}^g = 360)$ while keeping the mesh size $msh = 0,2\,mm$ for the three tests.

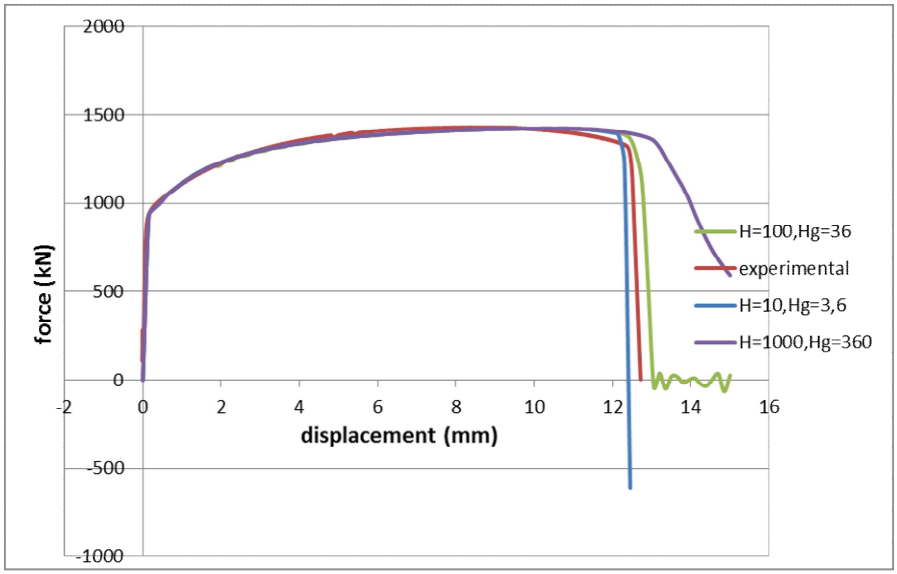

Figure 10. Comparison of the force-displacement curves for the three different couples $\breve{H}, \breve{H}^g$

$U_{rupt} = 12,3mm$

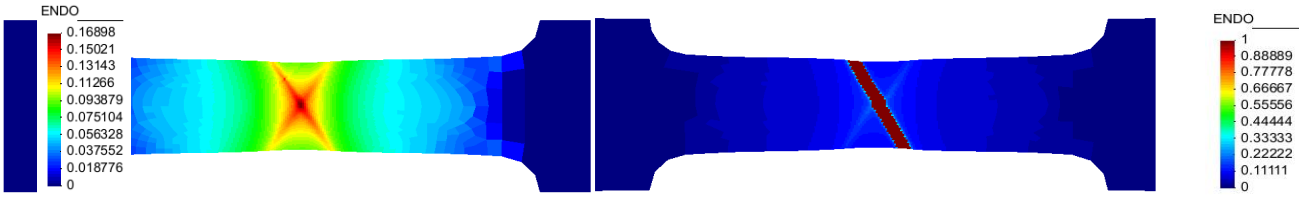

$U_{rupt} = 13,3mm$

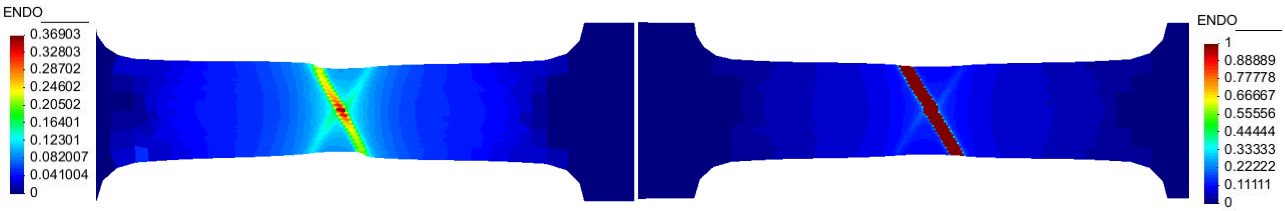

no final crack

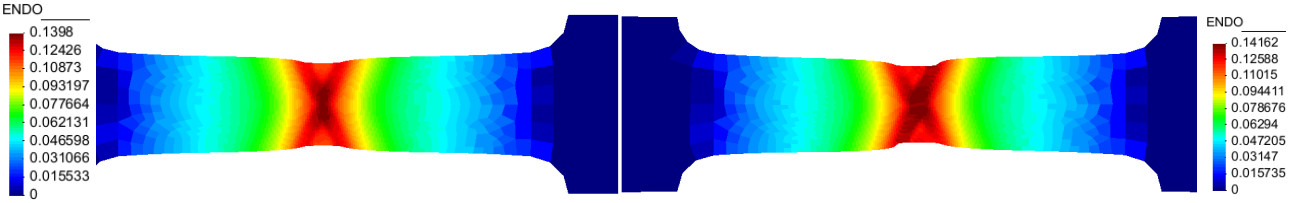

Figure 11. Damage isovalues of the ruptured specimen in the framework of the local continua

From Fig. 10 we can note that $\breve{H}$ has a preponderant effect on the elongation of the fructure. The bigger the value of $\breve{H}$ is, the more the rupture is delayed. In fact, $U_{rupt} = 12,3\,mm$ for $\breve{H} = 10$, $U_{rupt} = 13,3\,mm$ while we do not achieve any final rupture for the extremely high value of $\breve{H} = 1000$ due to the strong localized necking. Relatively low values of $\breve{H}$ give micromorphic responses close to the local one. This can be explained by the fact that Y_{nloc} is directly proportional to $\breve{H}$ in a way that low values of $\breve{H}$ lead to low values of Y_{nloc}.
Consequently, the most important parameter which influences the material ductility is the micromorphic modulus $\breve{H}$ which directly governs the damage energy release rate while the value of the modulus $\breve{H}^g$ affects the material ductility with a small amount by equally delaying the rupture displacement.

For the second test case, the effect of the mesh size is investigated. We keep the value of the internal length $\ell_{\breve{d}} = 0,6\,mm$ by choosing this couple of the micromorphic moduli $(\breve{H} = 100, \breve{H}^g = 36)$ and we perform the simulation for two different mesh sizes $msh = 0,2\,mm$ and $msh = 0,4\,mm$.

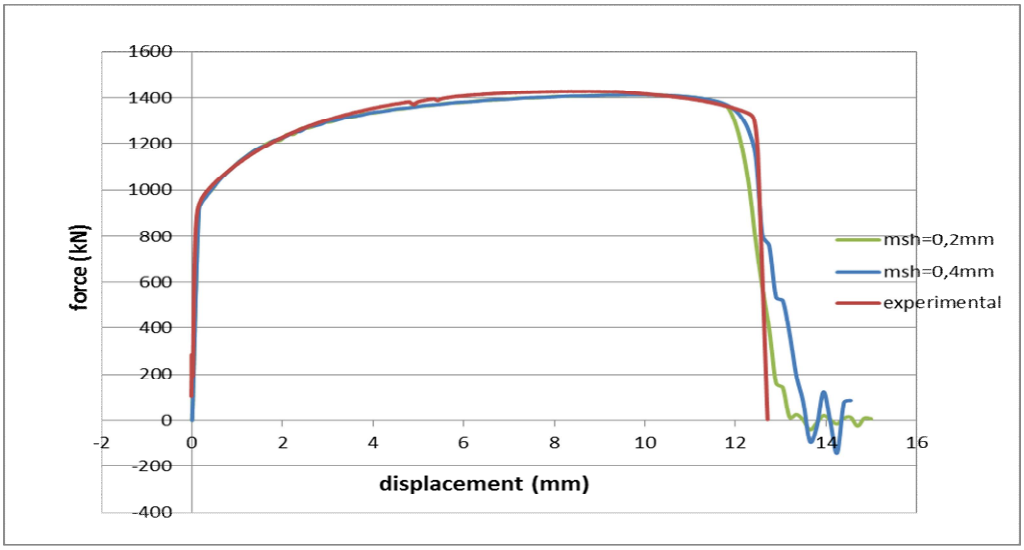

Figure 12. Comparison of the force-displacement curves for the two different mesh sizes.

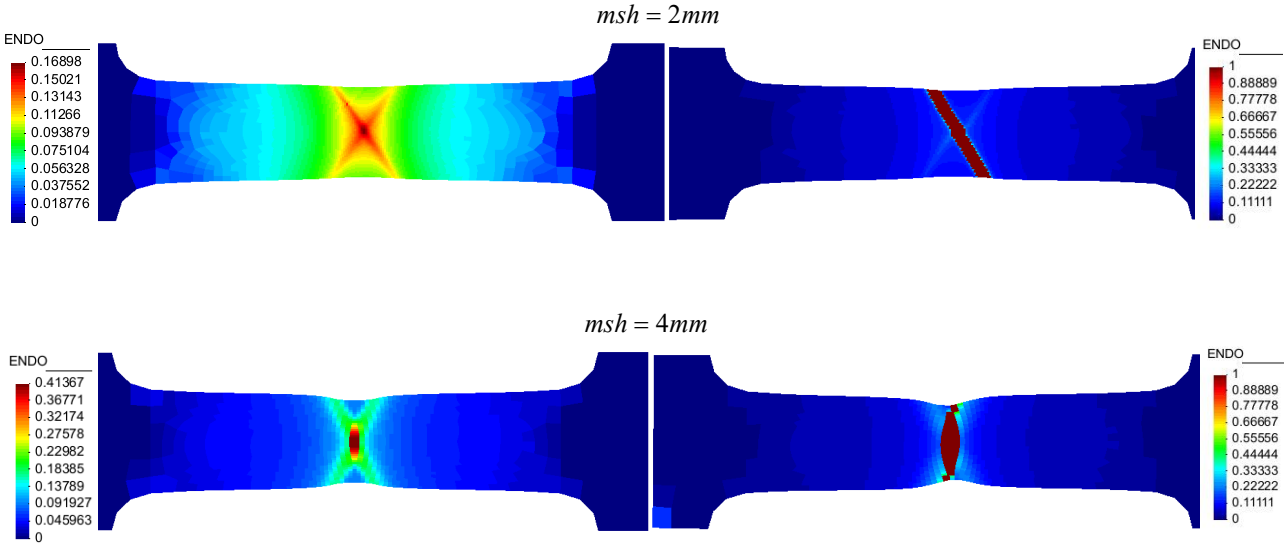

Figure 13. Damage isovalues of the ruptured specimen for the two different mesh sizes.

The corresponding results in terms of the damage distribution are plotted for the three mesh sizes in Fig. 13 From these figures it is clearly observed that the damage gradient is located inside a wide shear band. The force-displacement curve gives the same fracture displacement value $U_{rupt} \approx$ 13,3mm as shown in Fig. 12. However, we observe a slight difference between the three results in the softening phase. This difference can be explained by the need to introduce a micromorphic variable associated with the isotropic hardening in order to enhance the regularization at this stage (Saanouni and Hamed, 2013).
On the other hand, we can see that the orientation of the crack can be affected by the mesh size, something that poses difficulties to distinguish the dominant from the disappearing bands for the identification procedure discussed hereafter.

6 Identification Methodology

As mentioned in the fourth section above, generalized continua schemes introduce additional parameters that need special treatment for their identification. One of these is the internal length related to the micromorphic damage. Since ESPI allows the identification of the physical characteristics of the localization, such as bandwidths, band orientations and maximum strain rates of the bands at any moment of the necking, one first attempt is done under the idea of 'linking' the notion of the micromorphic internal length to the one of the bandwidths in order to give it some physical meaning and propose a numerical methodology to identify it.
In this spirit, and by numerically implementing the mathematical model given by Eqs. (26)-(28) and calculating the numerical strain rate at a given time $\dot{\varepsilon}_{xx}^{num}\left(x,y,t\right)$ at each Gauss point of an element located in the central zone and, we manage to extract the values of the numerical bandwidth B^{dom} during the diffuse and the localized necking and compare the numerical results with the experimental ones shown in Figure 8.

We manage to extract the values of the integral bandwidths during the diffused and the localized necking and compare the numerical results with the experimental ones shown in Fig. 8, first for the three different couples of the micromorphic moduli, $(\breve{H}=10,\breve{H}^{g}=3,6)$, $(\breve{H}=100,\breve{H}^{g}=36)$ and $(\breve{H}=1000,\breve{H}^{g}=360)$ and after for the two different mesh sizes $msh=0,2\,mm$ and $msh=0,4\,mm$.
Let us note that since the micromorphic isotropic hardening is not taken into account for this work, we proceed only to the identification of the internal length of the micromorphic damage and we associate to the dominant band named B^{dom} leading to the final rupture.

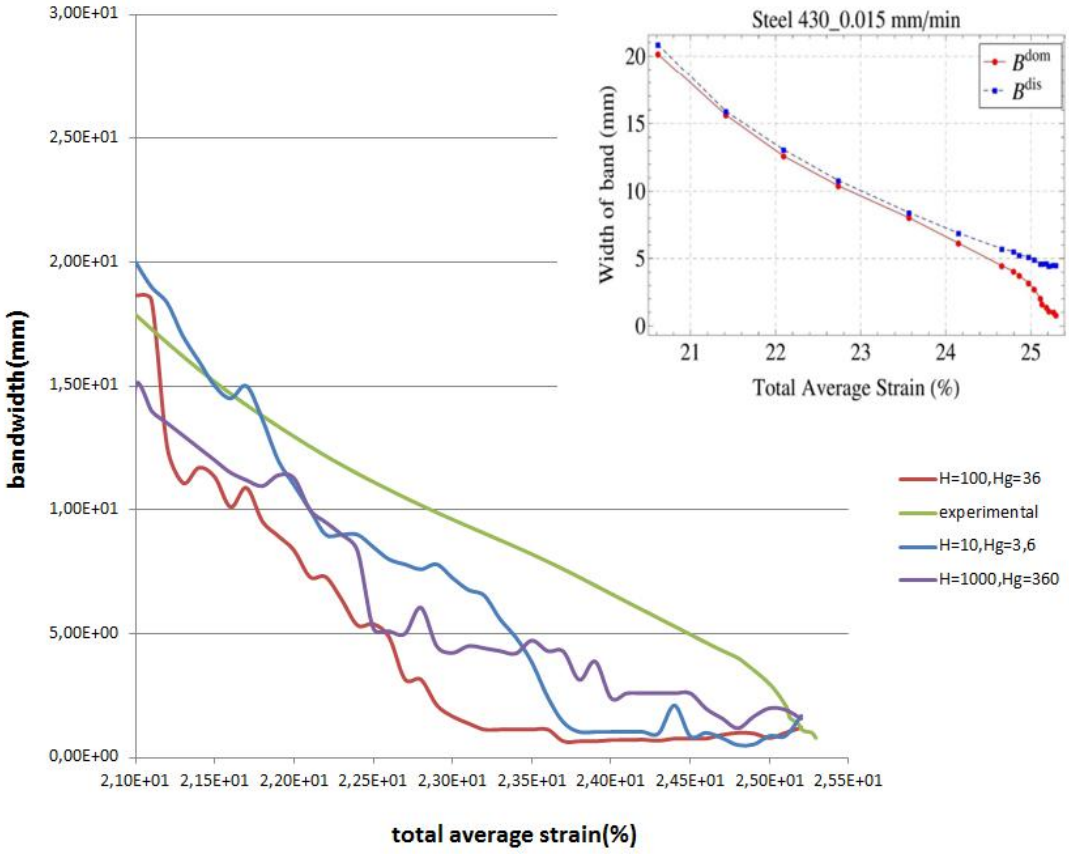

Figure 14. Evolution of the localization dominant band for a fixed mesh size, numerical-experimental comparison for $(\breve{H}=10,\breve{H}^g=3,6)$, $(\breve{H}=100,\breve{H}^g=36)$ and $(\breve{H}=1000,\breve{H}^g=360)$

Fig. 14 shows the numerical results obtained for the three pairs of the micromorphic moduli related to the micromorphic damage and its first gradient, $(\breve{H}=10,\breve{H}^g=3,6)$, $(\breve{H}=100,\breve{H}^g=36)$ and $(\breve{H}=1000,\breve{H}^g=360)$. Only the evolution of the dominant band associated to the micromorphic internal length is taken into consideration. The curves despite of being smoothened, still seem quite oscillating probably due to the dynamic effect. As shown from the numerical results, the width of B^{dom} at 25,5% of total average strain is around 0,2mm for all the cases which is in total agreement with the experiments. It is obvious that the higher the values of the micromorphic moduli are, the smaller becomes the bandwidth at 21% of the total average strain rangeing between 15mm for $(\breve{H}=1000,\breve{H}^g=360)$ and 20mm for $(\breve{H}=10,\breve{H}^g=3,6)$. For the third combination of $(\breve{H}=100,\breve{H}^g=36)$ the values of the bandwidth at the starting and the finishing point are almost identical however, the error between the numerical and the experimental curve is the biggest among the three tests.

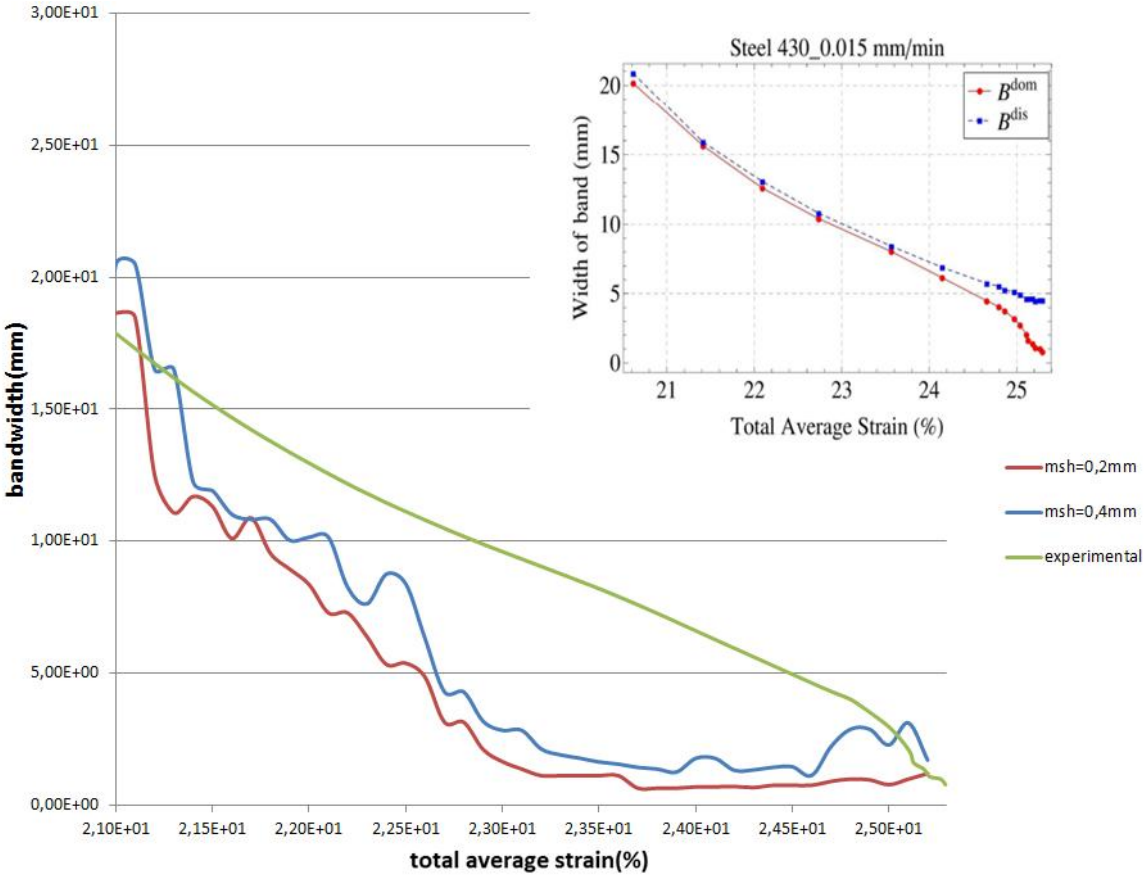

Figure 15. Evolution of the localization dominant band for $(\breve{H}=100, \breve{H}^g=36)$, numerical-experimental comparison for two varying meshes $msh=0,2\,mm$ and $msh=0,4\,mm$

Since the pair $(\breve{H}=100, \breve{H}^g=36)$ seems the most suitable and the one that is closer to the experimental results in the terms of the values of the bandwidth for the interval of the total average strain which is of main interest, we chose to use it and keep it constant while varying the mesh size two times at $msh=0,2\,mm$ and $msh=0,4\,mm$. It seems that the mesh size does not affect the evolution of the band and the tendency to decrease is respected as observed in the experiment. However, the bigger mesh of 0,4mm gives bigger value of the bandwidth at 21% as well as at 25,5% of the total average strain in contrast with the finer one where the values are in agreement with the experimental results.

For all the cases, the decreasing tendency is in agreement with the experimental results. We note that the parameter S is directly linked to the ductility and governs the apparition of the fracture after the diffuse necking. Meanwhile, it is observed that its effect is to delay or accelerate the damage growth without modifying the shape of the damage evolution or the $F-u$ curves.

For $S=4.5$ (used for all the tests presented) the widths evolve at a much lower level which does not allow an appropriate fitting. It is observed that the increase oft he parameter S leads to a better fitting by reducing the difference between the experimental and the numerical curves.

We note here that from the numerical point of view, for $h=0.4$ mm all the specimens failed at the opposite direction (see Fig. 13), so the experimental B^{dom} is represented by the numerical band B_2.

As a result from all the five cases tested, we can conclude that fine meshes and intermediate values of the micromorphic moduli (not extremely high that lead to strictions or relatively low approaching the local case) can provide a good agreement between the numerical and the existing experimental results and some useful information at first place for the identification of the micromorphic internal length and the justification of the choice of $\breve{H}$ and $\breve{H}^g$ at least for the current material used.

7 Conclusions and Future Works

In this paper we have formulated a micromorphic fully coupled damage model taking into account the strong coupling between all the mechanical fields and the micromorphic damage. As a result, a new variational form and a new balance equation that should be resolved simultaneously with the classical equilibrium equation is introduced. This model has been implemented in a Finite Element code into ABAQUS®/Explicit, by developing within the explicit dynamic global resolution scheme, a specific finite element as well as a local integration scheme and is successfully validated through a classical tensile test.
On the other hand, the micromorphic model, which has shown its ability to reduce the dependence of results against the mesh size, introduced a new parameter named as internal length of the material, which requires an experimental and numerical determination. For this need and by relying on the experimantal results coming from the speckle interferometry method, we introduce a numerical methodology in order to identify the appropriate value of the internal length related tot he micromorphic damage by trying to give it a physical meaning onnecting it to the widths of the shear bands.
Future works include the addition of more micromorphic degrees of freedom (e.g. micromorphic isotropic hardening) and extension of the model to the 3D case for various virtual metal forming processes.
Also, the improvement of the numerical results and the curve fitting of the proposed identification methodology as well as the identification of the micromorphic internal length related to the micromorphic isotropic hardening and its connection to the materials microstructures under large strains will be further investigated.

8 Acknowledgements

The financial support of ANR through the Program Micromorfing with the contract ANR-14-CE07-0035-01 and former Ph.D C.Bao (UTT/LASMIS) for the experimental work, are gratefully acknowledged.

References

Aifantis, E.C., 1987. The physics of plastic deformation. *Int. J. Plast*. 3, 211–248.

Aifantis, E.C., 2003. Update on a class of gradient theories. *Mech. Mater*. 35, 259–280.

Anand, L., Gurtin, M.E., Lele, S.P., Gething, C., 2005. A one-dimensional theory of strain-gradient plasticity: formulation, analysis, numerical results. *J. Mech. Phys. Solids* 53, 1789–1826.

Badreddine H, Saanouni K, Nguyen TD, *Damage anisotropy and its effect on the plastic anisotropy evolution under finite strains*, *International Journal of Solids and Structures* 63:11-31, 2015.

Cosserat, E., Cosserat, F., 1896. sur la Théorie de l'élasticité, *Annales de la Faculté des Sciences de Toulouse*, 1ére série, t.10, I.1–I.116.

Cosserat, E., Cosserat, F., 1909. Notes sur la théorie des corps déformables, in O.D. Chwolson, *Traité de Physique*, t.2, 953–1173, Hermann Librairie Scientifique, Paris.

Cosserat, E., Cosserat, F., 2009. *Théorie des corps déformables*, ISBN: 978 27056 6920 1, Hermann Editeurs, Paris.

Engelen, R., Geers, M.G.D., Baaijens, F., 2003. Nonlocal implicit gradient-enhanced elasto–plasticity for the modelling of softening behaviour. *Int. J. Plast*. 19, 403– 433.

Eringen AC. *Microcontinuum field theories*: I. Foundations and Solids. Springer Verlag, New York, 1999.

Eringen AC. *Nonlocal continuum field theories*. Springer Science & Business Media, 2002.

Eringen, A.C., 1966a. Linear theory of micropolar elasticity. *J. Math. Mech*. 15, 909–924.

Eringen, A.C., 1966b. Theory of micropolar fluids. *J. Math. Mech*. 16, 1–18.

Eringen, A.C., 1970. Balance laws of micromorphic mechanics. *Int. J. Eng. Sci*. 8, 819–828.

Eringen, A.C., 1999. *Microcontinuum Field Theories*: Foundation and Solids. Springer Verlag, New York.

Eringen, A.C., 2002. *Nonlocal Continuum Field Theories*. Springer Verlag, New York.

Eringen, A.C., Suhubi, E.S., 1964. Nonlinear theory of simple microelastic solids. *Int. J. Eng. Sci*. 2, 189–203, 389–404.

Forest S. *Milieux continus généralisés et matériaux hétérogènes*. Presses des MINES, 2006.

Forest, S., 2008. Some links between Cosserat, strain gradient crystal plasticity and the statistical theory of dislocations. *Phil. Mag*. 88 (30–32), 3549–3563.

Forest, S., 2009. Micromorphic approach for gradient elasticity, viscoplasticity and damage. *ASCE J. Eng. Mech*. 135 (3), 117–131.

Forest, S., Aifantis, E.C., 2010. Some links between recent gradient thermo–elasto–plasticity theories and the thermomechanics of generalized continua. *Int. J. Solids Struct*. 47, 3367–3376.

Forest, S., Sievert, R., 2003. Elastoviscoplastic constitutive frameworks for generalized continua. *Acta Mech*. 160, 71–111.

Forest, S., Sievert, R., 2006. Nonlinear microstrain theories. *Int. J. Solids Struct*. 43, 7224–7245.

Forest, S., Sievert, R., Aifantis, E.C., 2002. Strain gradient cristal plasticity: thermomechanical formulations and applications. *J. Mech. Behav. Mater*. 13, 219–232.

Geers, M.G.D., 2004. Finite strain logarithmic hyperelasto–plasticity with softening: a strongly non-local implicit gradient framework. *Comput. Methods Appl. Mech. Eng*. 193, 3377–3401.

Geers, M.G.D., Ubachs, R., Engelen, R., 2003. Strongly non-local gradient-enhanced finite strain elastoplasticity. *Int. J. Numer. Methods Eng*. 56, 2039–2068.

B Guelorget, M François, C Vial-Edwards, G Montay, L Daniel, J Lu. Strain Rate Measurement by Electronic Speckle Pattern Interferometry: A New Look at the Localization Onset. *Materials Science and Engineering*: A. 2006; 415: 234-241.

Hirschberger, C.B., Steinmann, P., 2009. Classification of concepts in thermodynamically consistent generalized plasticity. *ASCE J. Eng. Mech*. 135 (3), 156–170.

Issa M, Labergère C, Saanouni K, Rassineux, A Numerical prediction of thermomechanical field localization in orthogonal cutting, *CIRP Journal of Manufacturing Science and Technology* 5 (3):175-195, 2012.

J. Wang, J. Chen, M. Li, *A URI 4-Node quadrilateral element by assumed strain method for nonlinear problems* (Allerton Press, INC., New York, U.S.A, 2006), *ACTA MECHANICA SNICA*, Vol.20, No.6, December 2004.

K. Saanouni, M. Hamed, Micromorphic approach for finite gradient-elastoplasticity fully coupled with ductile damage: Formulation and computational aspects, *Int. J. of Solids and Structures* 50(S 14–15), pp. 2289–2309, 2013.

Kirchner, N., Steinmann, P., 2005. A unifying treartise on variational principles for gradient an micromorphic continua. *Phil. Mag*. 85 (33–35), 3875–3895.

Labergère C, Rassineux AA, Saanouni KK, 2D adaptive mesh methodology for the simulation of metal forming processes with damage*, International journal of material forming* 4 (3):317-328, 2011.

Liebe, T., Menzel, A., Steinmann, P., 2003. Theory and numerics of geometrically nonlinear gradient plasticity. *Int. J. Eng. Sci*. 41, 1603–1629.

Maugin, G., 1979. Nonlocal theories or gradient-type theories: a matter of convenience? *Arch. Mech*. 31, 15–26.

Mindlin, R.D., 1964. Micro-structure in linear elasticity. *Arch. Rat. Mech. Anal*. 16, 51–78.

Mindlin, R.D., 1965. Second gradient of strain and surface–tension in linear elasticity. *Int. J. Solids Struct*. 1, 417–438.

Mindlin, R.D., Eshel, N.N., 1968. On first strain gradient theories in linear elasticity. *Int. J. Solids Struct*. 4, 109–124.

Nedjar, B., 2001. Elastoplastic-damage modelling including the gradient of damage: formulation and computational aspects. *Int. J. Solids Struct*. 38, 5421–5451.

Saanouni K, Badreddine H, Ajmal M, Advances in virtual metal forming including the ductile damage occurrence: Application to 3D sheet metal deep drawing, *Journal of engineering materials and technology* 130 (2):02102201-02102211, 2008.

Saanouni K, Chaboche J, *Computational damage mechanics. Application to metal forming,* Numerical and Computational Methods in Comprehensive Structural Integrity 3, 2003.

Saanouni K, Cherouat A, Hammi Y, Numerical aspects of finite elastoplasticity with isotropic ductile damage for metal forming, *Revue européenne des éléments finis* 2-3-4:327-351, 2001.

Saanouni K, Hammi Y, Numerical simulation of damage in metal forming processes, Elsevier, New York, 2000.

Saanouni K, Nesnas K, Hammi Y, Damage modeling in metal forming processes, *International Journal of Damage Mechanics* 9 (3):196-240, 2000.

Saanouni K. *Damage mechanics in metal forming: advanced modeling and numerical simulation*. John Wiley & Sons, 2012.

Saanouni, K., Forster, C., Benhatira, F., 1994. On the anelastic flow with damage. *Int. J. Damage Mech*. 3 (2), 40–169.

Sidoroff, F., 1975. Microstructure and plasticity. *Mech. Res. Commun*. 2, 73–77.

Simo J.C., Hughes T.J.R, *Computational inelasticity*, (Springer Verlag, New York), 1998.
Springer-Verlag, New York.

T. Belytscho, W.K. Liu, B. Moran, *Nonlinear Finite Elements for Continua and Structures* (John Wiley & Sons Ltd, The Atrium, Southern Gate, Chichester, West Sussex, England , 2000).

Truesdell, C., Noll, W., 2004. *The Nonlinear Filed Theories of Mechanics*, third ed.

Truesdell, C., Noll, W., 2004. *The Nonlinear Filed Theories of Mechanics*, third ed. Springer-Verlag, New York.

Address*:* University of Technology of Troyes, ICD/LASMIS UMR-CNRS 6281, 12 rue Marie Curie CS 42060 Troyes Cedex, France
email: evangelia.diamantopoulou@utt.fr